Solar-driven production of hydrogen and acetaldehyde from ethanol on Ni-Cu bimetallic catalysts with solar-to-fuels conversion efficiency up to 3.8%

Shunqin Luo, [ab‡] Hui Song, [ab‡] Davin Philo, [ab] Mitsutake Oshikiri, [c] Tetsuya Kako, [b] and Jinhua Ye *[abde]

[a] Graduate School of Chemical Sciences and Engineering, Hokkaido University, Sapporo 060-0814, Japan

[b] International Center for Materials Nanoarchitectonics (WPI-MANA), National Institute for Materials Science (NIMS), 1-1 Namiki, Tsukuba, Ibaraki 305-0044, Japan

[c] International Center for Materials Nanoarchitectonics (WPI-MANA), National Institute for Materials Science (NIMS), 3-13 Sakura, Tsukuba, Ibaraki 305-0003, Japan

[d] TJU-NIMS International Collaboration Laboratory, School of Material Science and Engineering, Tianjin University, Tianjin 300072, P. R. China

[e] Collaborative Innovation Center of Chemical Science and Engineering (Tianjin), Tianjin 300072, P. R. China

‡ These authors contributed equally to this work.

Abstract

Catalytic ethanol dehydrogenation is recognized as a promising approach to produce valuable chemical stocks, yet its industrialization suffers from high energy consumption. Here, we present an efficient solar-driven ethanol dehydrogenation process using a low-cost Ni-Cu bimetallic catalyst for the high-yield and selective production of H_2 and acetaldehyde. Under the irradiation of focused simulated solar light, 176.6 mmol $g_{catalyst}^{-1}$ h^{-1} of H_2 production rate with a high solar-to-fuel conversion efficiency (3.8%) was achieved without additional thermal energy input, which is far more efficient than any previously reported photocatalytic ethanol dehydrogenation systems. Mechanistic investigations revealed that photothermal heating and hot carrier

generation over Ni-Cu catalysts took responsibilities for the high activity. Hot electrons generated from Cu nanoparticles could migrate to Ni atoms, which simultaneously favored the separation of charge carriers and the activation of adsorbates. This study opens a promising pathway toward solar-energy conversion technology and advanced cost-effective industrial processes.

Keywords: Solar-driven photocatalysis; Ethanol dehydrogenation; Ni-Cu bimetallic catalysts; Solar-to-fuel conversion; Hot electrons

1. Introduction

Hydrogen (H_2) is an important chemical and fuel which can be utilized for many applications, such as hydrogenation reaction and fuel cell [1-3]. To date, large-scale hydrogen production in the industry is primarily through steam methane reforming; however, this process requires high operating temperatures (700-1100 °C), thus consuming a massive amount of energy [4]. Since solar light is by far the greatest available source of renewable energy, the utilization of solar energy to drive the chemical reactions, so-called photocatalytic process, is attractive for its sustainability [5, 6]. Photocatalytic H_2 production from ethanol dehydrogenation ($CH_3CH_2OH \rightarrow CH_3CHO + H_2$, $\Delta H = 68$ kJ mol^{-1}) is a promising alternative approach because only solar light is employed as the energy input and ethanol can be produced from renewable biomass [7]. In addition, the other product, acetaldehyde is one of the important building blocks for the synthesis of various industrial chemicals [8, 9]. This reaction has been intensively studied by using various semiconductors and/or metals in these recent years [7, 10-12], however, the reported efficiencies are still quite low (remains only several mmol $g_{catalyst}^{-1}$ h^{-1} level with low solar-to-fuel conversion efficiency), rendering no any potential industrial applications [13, 14]. Up until now, in order to obtain a satisfactory production rate in the photocatalytic ethanol dehydrogenation system, thermal energy is still required as the main energy input to drive the reaction [15]. In this case, a significant breakthrough is necessary to manifest the efficient solar-driven ethanol dehydrogenation system (without any thermal energy input) for prospective and cost-effective industrial processes.

Recently, light-harvesting plasmonic metal nanostructures have attracted much research interests [16-18]. Compared with the traditional photocatalytic process, the full solar spectrum, including the ultra-violet (UV), visible, and even near-infrared (NIR) light can be utilized by plasmonic metal catalysts to drive catalytic reactions [19]. With the assistance of light, plasmonic photocatalysts can drive many reactions with enhanced activities under far milder conditions compared to conventional thermocatalysis [20, 21]. The strong interaction between photon energy and plasmonic metal nanostructures through the excitation of localized surface plasmon resonance (LSPR) generates energetic hot carriers, which can drive reactions by locally heating nanoparticles and/or transferring the energy into reactants for synergistically enhancing the catalytic activity [22]. Plasmonic metal nanoparticles such as Au, Ag, Cu have been employed as catalysts in various chemical reactions such as carbon dioxide reduction and methane reforming reactions [23-27]. Among all the plasmonic metals, Cu is a promising candidate for practical application due to its low cost and unique properties [28-30]. Recently, Halas and her colleagues demonstrated that hot carriers and photo-thermal effect could be produced simultaneously by the illumination of plasmonic Cu-Ru nanoparticles for reducing the reaction activation barrier [16]. In addition, Cu-based nanomaterials are also good candidate catalysts for thermal catalytic ethanol dehydrogenation [31-33]. It was reported that Cu-Ni single atom alloy catalysts could exhibit good activity and stability towards thermal catalytic ethanol dehydrogenation reaction, where Ni single atom would improve the activity and stability of Cu nanoparticles [34]. Nevertheless, this process still required a relatively high operating temperature (~ 300 °C).

In this study, we demonstrate an efficient solar-driven ethanol dehydrogenation process for the production of H_2 and acetaldehyde over plasmonic Ni-Cu bimetallic catalysts. Under the illumination of simulated 5.7 Suns with no external energy input, a superior H_2 production rate of 176.6 mmol $g_{catalyst}^{-1}$ h^{-1} with 3.81% of solar-to-fuel conversion efficiency is obtained. Mechanistic investigations indicate that photothermal heating and hot carrier generation over Ni-Cu catalysts take responsibility

for the high activity. The apparent activation energy for ethanol dehydrogenation reaction is reduced by ~55% over Ni-Cu bimetallic catalysts under visible light irradiation compared to the pure Cu under dark condition. *In-situ* DRIFTS results reveal that the adsorbed intermediates could be activated by the photo-induced hot carriers. First-principles molecular dynamics simulation results suggest that the hot electrons produced by Cu nanoparticles easily migrate to Ni atoms and then transfer to the adsorbates, hence suppressing the non-effective carrier recombination and leading to the promotion of hydrogen production.

2. Experimental section

2.1 Catalysts preparation

Cu nanoparticles were synthesized by using the wet chemistry method [32]. Accordingly, 0.1 M (10 mL) ascorbic acid (L(+)-Ascorbic acid, Wako, 99% purity, CAS: 50-81-7) solution was added into a mixed aqueous solution (100 mL) of Cu $(NO_3)_2 \cdot 3H_2O$ (Copper nitrate trihydrate, Wako, 99% purity, CAS: 10031-43-3) and PVP (Polyvinylpyrrolidone, Sigma-Aldrich, CAS: 9003-39-8) (200:1 molar ratio of Cu to PVP). 500 mg of SiO_2 (Silicon dioxide, Wako, 99.9% purity, CAS: 7631-86-9) was then added into the solution, under continuous stirring to form a homogeneous dispersion. Afterward, 0.1 M (10 mL) of $NaBH_4$ (Sodium tetrahydroborate, Wako, 95% purity, CAS: 16940-66-2) was drop-wisely added into the solution. The solution was stirred continuously at room temperature in the Ar atmosphere to prevent the oxidation of Cu. After stirred for 1 h, the solid was collected and washed by ethanol and water three times, followed by drying in a vacuum oven in 70 °C overnight and calcination in the air at 350 °C for 4 h. The sample was reduced in hydrogen (10% in Ar) at 350 °C for 3 h to prepare SiO_2 supported metallic Cu nanoparticle (named as Cu here and after). Ni atoms were deposited on Cu by using electroless galvanic deposition method [34], based on the following reaction:

$$2Cu + 2OH^- + Ni^{2+} = Cu_2O + Ni + H_2O, \Delta E^0 = +0.103\,V$$

The Cu atom can be substituted by Ni in alkaline solution spontaneously with the oxidation of the Cu. The fabrication process (Scheme S1) was shown as follows: pH value of Ni $(NO_3)_2 \cdot 3H_2O$ (Nickel nitrate hexahydrate, Wako, 99% purity, CAS: 13478-00-7) aqueous solution was adjusted to 10.83 by drop-wise adding 0.01 M NaOH (Sodium Hydroxide, Wako, 97% purity, CAS: 1310-73-2) under Ar protection and continuous stirring. Subsequently, a certain amount of Cu was added into the solution, and keep stirred under Ar protection for 1 h. The precipitates were collected by using a centrifuge, washed with deionized water three times and then dried at 70 °C in vacuum overnight. The catalysts were then reduced in hydrogen (10% in Ar) at 400 °C for 1 h. The typical atomic ratio of Ni in Cu ranges from 0.04 to 0.18, as determined by the inductivity coupled plasma optical emission spectrometer (ICP-OES). For comparison, pure Ni catalysts were synthesis by the same method as the fabrication process of Cu, and the Ni $(NO_3)_2 \cdot 3H_2O$ was utilized as the nickel source.

2.2 Characterization

The crystalline structures of the catalysts were characterized using an X-ray powder diffractometer with Cu Kα radiation (PANalytical). The surface electronic states of catalysts were investigated by X-ray photoelectron spectroscopy (XPS, Escalab 250 Xi, Thermo Scientific). UV-Vis absorption spectra of catalysts were collected by a spectrophotometer (UV-2600, Shimadzu). Transmission electron microscopy (TEM) and high-resolution TEM (HRTEM) measurements were carried out on the FEI TECNAI G2 F30 instrument. Scanning transmission electron microscope energy dispersive X-ray spectrometry (STEM-EDS) mapping analysis was conducted on a FEI Titan Cubed instrument. Light intensity and wavelength distribution of the illuminant were analyzed by the USR-40 spectrophotometer. Diffuse reflectance infrared Fourier transform spectroscopy (DRIFTS) measurements were performed on a FT-IR-6300 system (JASCO Corp.) equipped with an *in-situ* DR cell and a liquid nitrogen-cooled mercury-cadmium-telluride detector. For CO-DRIFTS, 10 mg samples were firstly reduced in the reaction cell in a hydrogen atmosphere at 350 °C for 1 h. After the reduction, the samples were purged with Ar gas. Background spectra were recorded in

the Ar atmosphere after the catalysts cooling down to room temperature. CO gas (2% in Ar) was introduced into the cell for 20 min at a flow rate of 10 mL min^{-1}, then the gas was switched to Ar flowing at 20 mL min^{-1}. After Ar gas purged for 5 min and 15 min, spectra were recorded.

2.3 Photocatalytic activity measurements

Two different types of reactors (solar-driven catalysis reactor and photo-assisted thermal catalysis reactor) were utilized to manifest the solar-driven catalytic activity and reaction mechanism, respectively. Solar-driven ethanol dehydrogenation reaction was conducted in a home-made flow-type reactor (diameter 10 mm) with quartz cover to allow the irradiation of light to catalysts (Figure S1). In this measurement, the AM 1.5 light was employed as the illuminant, and no external thermal energy was applied. A maximum light intensity of 574 mW cm^{-2} was achieved by the optical lens (Figure S2). A thermocouple was utilized to test the surface temperature of catalysts. Prior to the activity measurement, the catalysts (10 mg) were reduced at 350 °C for 1 h under a flow of hydrogen (10% in Ar), then dispersed in the reaction cell uniformly after cooling down to the room temperature. Through a bubbler system, the reaction gas (5.6% ethanol balanced in Ar) was introduced into the reactor. The space velocity was controlled to be 50 mL min^{-1} unless otherwise specified. The products were quantified by gas chromatography (GC) equipped with thermal conductivity and flame ionization detector.

The solar-to-fuel (STF) efficiency in different light intensity was calculated by the following formula [35]:

$$STF = [r(H_2) \times \Delta_f G^0_{H_2} + r(C_2H_4O) \times \Delta_f G^0_{C_2H_4O} - r(C_2H_6O) \times \Delta_f G^0_{C_2H_6O}]/P_{\text{irradiation}} \times 100\%$$

The standard molar Gibbs energies of formation (Δ_fG^0) for H_2, C_2H_4O, and C_2H_6O ($\Delta_fG^0_{H2}$, $\Delta_fG^0_{C2H4O}$, and $\Delta_fG^0_{C2H6O}$) are 0, -133.0 and -167.9 kJ mol^{-1} [35, 36], $P_{irradiation}$: the power of light irradiation. In our reaction, only trace amount of CO and CH_4 were generated, indicating the selectivity of this reaction was nearly 100%. Therefore, the $r(H_2)$, $r(C_2H_4O)$ and $r(C_2H_6O)$ were considered to be the same in the STF calculation.

In order to elucidate the reaction mechanism, photo-assisted thermal catalytic ethanol dehydrogenation reaction was conducted under atmospheric pressure in a homemade flow-bed reactor (diameter 8.5 mm), as shown in Figure S3. A quartz window was equipped on the reactor to allow the irradiation of visible light to the catalysts. LA-251 Xe lamp with HA30 and L42 filters (to remove the infrared and ultra-violate light) was employed to provide the photon energy (Figure S4). The thermocouple and temperature controller (TC-1000, JASCO) were utilized to keep the catalysts at the desired temperature (Figure S5). Heat induced by light irradiation was be mitigated by the temperature controller (Figure S6). Typically, 5 mg of catalysts were dispersed in the reaction cell uniformly. Prior to the activity measurement, the catalysts were *in-situ* reduced in the reactor at 350 °C for 1 h under a flow of hydrogen (10% in Ar), then cooling down to the room temperature. Subsequently, the reactor was flushed with pure Ar gas for 30 min to remove the hydrogen in the reactor. The reaction gas was introduced into the reactor at a flow rate of 50 mL min^{-1} through the bubbler system. The product measurement method was as same as the solar-driven ethanol dehydrogenation reaction.

2.4 *In-situ* DRIFTS analysis

FT-IR-6300 system (JASCO Corp.) equipped with an *in-situ* DR cell and a liquid nitrogen-cooled mercury-cadmium-telluride detector was utilized to elucidate the reaction role of photo-induced hot carriers at 200 °C (Figure S7). In DRIFTS measurement, 10 mg of $Ni_{0.04}Cu$ were dispersed uniformly in the DR cell, and in-situ reduced under a flow of hydrogen (10% in Ar) at 350 °C for 1 h. After cooling down to the room temperature, pure Ar gas was introduced to remove the hydrogen, followed by the introduction of Ar (20 mL min^{-1}) at 200 °C to get the background spectrum of the system. The DRIFT spectra during the reaction were recorded after the reaction gas was introduced in the reaction cell at 200 °C with the irradiation of visible light for 15 min.

2.5 Computational details

First-principles molecular dynamics simulation [37] and the electronic structure calculations based on the density functional theory within local density approximation (DFT-LDA) were carried out to demonstrate the transfer process of electrons excited from the Cu-based nanoparticles to adsorbate materials. To mimic the Ni surficially doped Cu nanoparticles loaded on a SiO_2 supporter material in presence of gas-phase ethanol (CH_3CH_2OH) molecules, we employed the simulation model including a slab of metal Cu, which was doped with Ni atoms only at the slab surface (184 Cu and 8 Ni), at the bottom of the supercell and the reactant molecules of ethanol ($4CH_3CH_2OH$) in the space above the slab mimicking a gas phase. The detailed model specifications were described blow. Employing the model, the first-principles quantum molecular dynamics simulation (CPMD) was achieved, and have obtained the equilibrium structure of the system at 200 °C (473 K). Then the electronic structure was computed by solving the Kohn-Sham equation within LDA.

2.6 Computational model

Cu metal crystal with face-centered cubic lattice, whose lattice length a is 3.615 Å (ICSD code 627114), was quarried in the size of 4a (14.460 Å) × 4a × 3a (10.845 Å) and was placed at the bottom of the simulation cell whose size was 4a × 4a × 20 Å. The eight surficial Cu atoms at the (001) surface were randomly exchanged for Ni. Then the four ethanol molecules were put in the open space (~ 11 Å in thickness) of the cell with moderate distances kept between molecules each other and between the slab surface and the molecules to avoid undesirable bias. The number of atoms of Cu, Ni, C, O, and H included in the cell box were 184, 8, 8, 4, and 24, respectively.

3 Results and discussion

3.1 Characterization of catalysts

The X-ray powder diffractometer (XRD) pattern of pure Cu and Ni-Cu bimetallic catalysts were presented in Figure 1a. The XRD pattern of Cu catalysts was dominated by the diffraction peaks of metallic Cu, revealing that the metallic Cu were synthesized successfully. No diffraction peak could be observed for Ni in Ni-Cu bimetallic catalysts,

indicating the small particle size and low contents of Ni. As determined by the inductivity coupled plasma optical emission spectrometer (ICP-OES), the typical atomic ratio of Ni in Cu ranges from 0.04 to 0.18 (Table S1). Transmission electron microscopy (TEM) images of $Ni_{0.04}Cu$ show that the Cu nanoparticles were dispersed on the surface of SiO_2 supporter, and the average particle size of Cu was approximately 30 nm (Figure 1b). A clear lattice fringe was measured to be 0.21 nm, which was in good agreement with the interplanar distance of the (110) plane of metallic Cu (Figure 1c). Scanning transmission electron microscope energy dispersive X-ray spectrometry (STEM-EDS) mapping of $Ni_{0.04}Cu$ (Figure S8) showed that no Ni signal could be detected in the STEM-EDS mapping analysis, which could be attributed to the low contents of Ni. However, the map sum spectrum (Figure S8e) indicated the presence of Ni in $Ni_{0.04}Cu$, since the weak peaks of Ni were observed.

The X-ray photoelectron spectroscopy (XPS) spectra of Cu and Ni were presented in Figure 1d and e. In the Cu 2p spectrum, two peaks at 934.8 eV and 933.2 eV were observed, which could be attributed to the Cu^{2+} and metallic Cu, respectively [3]. The existence of Cu^{2+} could be ascribed to the oxidization of catalysts exposed in the air. Ni 2p XPS spectra indicated that Ni^{2+} is the dominant species, which could be attributed to the highly dispersed metallic Ni on the surface of Cu can be easily oxidized into NiO in the air [32]. The optical properties of pure Cu and $Ni_{0.04}Cu$ catalysts were measured using UV-Vis diffuse reflectance spectra (UV-Vis DRS). As shown in Figure 1f, the wide absorption peak at a wavelength of 580 nm was observed for the pure Cu catalysts, which could be assigned to the LSPR peak of Cu [38]. After the deposition of Ni on the surface of Cu, the position of absorption peak remains unchanged.

In order to further elucidate the dispersion of Ni on Cu nanoparticles, CO was employed as a probe molecule in the DRIFTS measurement. In general, single atoms from nanoparticles can be directly identified by using CO in the DRIFTS measurement [39-43]. It is an effective characterization method and provides solid evidence for the formation of single atoms. CO-DRIFT spectra of pure Cu in the CO related region (Figure 1g) showed one peak at 2128 cm^{-1}, which could be assigned to CO binding to

Cu atom [44]. On the other hand, in the $Ni_{0.18}Cu$ CO-DRIFT spectra (Figure 1h), the main peak was observed at 2110 cm^{-1}, which may be related to the adsorption of CO on Ni nanoparticle. The existence of a linear CO adsorption peak at ~2055 cm^{-1} indicated the presence of Ni nanoparticles in $Ni_{0.18}Cu$ [45]. Compared with pure Cu and $Ni_{0.18}Cu$, $Ni_{0.04}Cu$ (Figure 1i) displayed the main peak at 2128 cm^{-1} and a shoulder peak at 2110 cm^{-1}, while the linear CO adsorption peak was completely absent. The additional shoulder peak at 2110 cm^{-1} could be attributed to Ni(CO)x sub-carbonyl species with x = 2 or 3 [32, 45]. CO-DRIFT spectra of $Ni_{0.04}Cu$ indicated that Ni atoms were atomically dispersed on Cu nanoparticles.

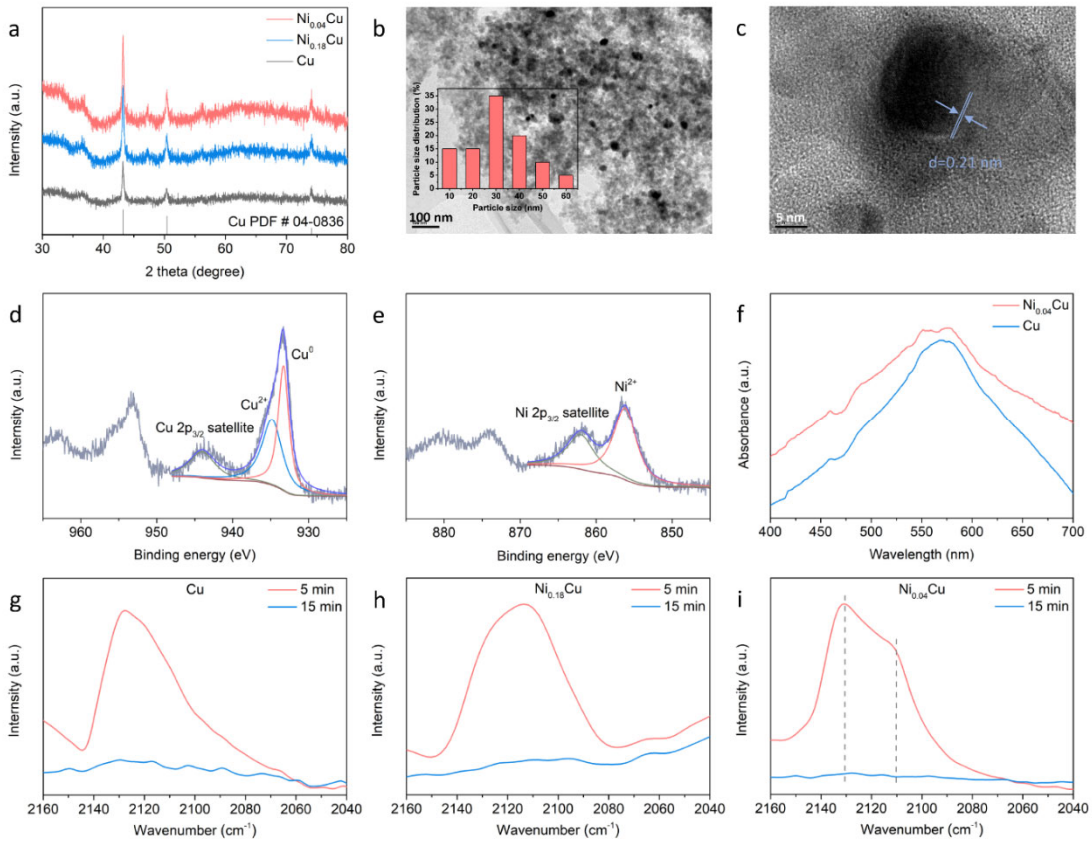

Figure 1. Characterization of Ni-Cu bimetallic catalysts. (a) XRD patterns of pristine Cu and Ni-Cu bimetallic catalysts, (b and c) TEM and HRTEM images of $Ni_{0.04}Cu$ catalysts, (d and e) XPS patterns of $Ni_{0.04}Cu$ catalysts, (f) UV-Vis DRS patterns of pristine Cu and Ni-Cu bimetallic catalysts, (g) CO-DRIFT spectra of pristine Cu catalysts, (h) CO-DRIFT spectra of $Ni_{0.18}Cu$ catalysts, (i) CO-DRIFT spectra of $Ni_{0.04}Cu$ catalysts.

3.2 Solar-driven ethanol dehydrogenation reaction over Ni-Cu bimetallic catalysts

Solar-driven ethanol dehydrogenation reaction over Ni-Cu bimetallic catalysts was performed on a home-made flow-bed reactor under atmospheric pressure. The AM 1.5 light was employed as the illuminant. An optical lens was utilized to focus the light. Maximum light intensity was measured to be 574 mW cm^{-2} (~ 5.7 suns). As shown in Figure 2a, with the increasing light intensity, the surface temperature of catalysts increased linearly. A surface temperature of 209 °C was achieved on the $Ni_{0.04}Cu$ at maximum light intensity (Figure 2a). Roughly the same temperatures were detected on the surface of $Ni_{0.04}Cu$, $Ni_{0.18}Cu$, and Cu. Figure 2b showed that under the irradiation intensity of 289 mW cm^{-2}, $Ni_{0.04}Cu$ exhibited H_2 production rate of 115 μmol $g_{catalyst}^{-1}$ min^{-1}, which was higher than pure Cu (66 μmol $g_{catalyst}^{-1}$ min^{-1}). The reaction rate was increased exponentially with the increasing light intensity. The H_2 production rate of $Ni_{0.04}Cu$ increased to 2943 μmol $g_{catalyst}^{-1}$ min^{-1}, corresponding to 176.6 mmol $g_{catalyst}^{-1}$ h^{-1}, with the light intensity increasing to 574 mW cm^{-2}, while the pure Cu only displayed the reaction rate of 1281 μmol $g_{catalyst}^{-1}$ min^{-1} at a same light intensity. This result illustrated that after adding a little amount of Ni on Cu, $Ni_{0.04}Cu$ showed much higher activity than pure Cu towards ethanol dehydrogenation reaction. Further increasing Ni contents could decrease the catalytic ethanol dehydrogenation activity of Ni-Cu bimetallic catalysts. Compared with $Ni_{0.04}Cu$ (2943 μmol $g_{catalyst}^{-1}$ min^{-1} at 574 mW cm^{-2}), $Ni_{0.18}Cu$ displayed lower activity (2125 μmol $g_{catalyst}^{-1}$ min^{-1}). This result suggested that atomic dispersed Ni significantly promoted the solar-driven catalytic activity of Ni-Cu bimetallic catalysts. Compared with representative works, Ni-Cu bimetallic catalysts presented high activity towards photocatalytic ethanol dehydrogenation (Table S2). Figure 2c showed that the solar-to-fuel (STF) efficiency increased with the increasing light intensity. The efficiency of $Ni_{0.04}Cu$ reached about 3.81% when the light intensity was 574 mW cm^{-2}. In addition, the reaction rate in different space velocity (Figure 2d) of $Ni_{0.04}Cu$ showed that the reaction rate increased with the increasing space velocity in the low space velocity area (10-50 mL min^{-1}). The H_2

production rate reached maximum value under the space velocity of 50 mL min^{-1}. When the space velocity further increased, the reaction rate remained nearly unchanged.

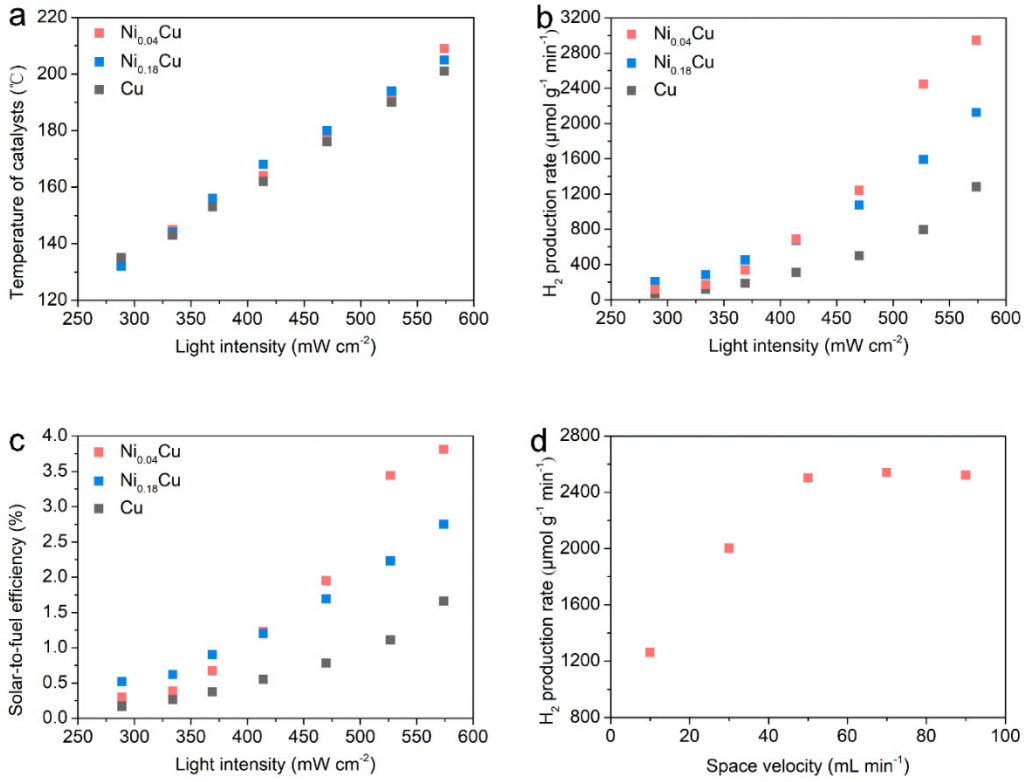

Figure 2. Solar-driven ethanol dehydrogenation reaction over Ni-Cu bimetallic catalysts. (a) Dependence of surface temperature of pure Cu and Ni-Cu bimetallic catalysts on different light intensity, (b) Solar-driven ethanol dehydrogenation activity over pure Cu and Ni-Cu bimetallic catalysts, (c) Solar-to-fuel efficiency of pure Cu and Ni-Cu bimetallic catalysts, (d) Dependence of H_2 production rate of $Ni_{0.04}Cu$ on different space velocity under the irradiation intensity of 527 mW cm^{-2}.

3.3 Mechanism for hot carriers assisted ethanol dehydrogenation reaction

Photo-assisted thermal catalytic ethanol dehydrogenation reaction was performed on a flow-bed reactor under atmospheric pressure to elucidate the reaction mechanism of hot carriers. To rule out the influence of UV and IR light, only visible light ($420 < \lambda < 800$ nm) with an intensity of ~440 mW cm^{-2} was used in the measurement (Figure S9).

As shown in Figure 3a, under the dark conditions, the H_2 production rate of pure Cu and Ni-Cu bimetallic catalysts increased with increasing reaction temperature. The H_2 production rate of $Ni_{0.04}Cu$ was increased from 264.3 μmol $g_{catalyst}^{-1}$ min^{-1} to 1192.0 μmol $g_{catalyst}^{-1}$ min^{-1} with the increasing temperature from 170 °C to 210 °C, which is higher than the pure Cu at the same reaction temperature. Moreover, the reaction rate could be further promoted after introducing photon energy. As shown from Figure 3a, under the visible light irradiation with the reaction temperature of 170 °C, the H_2 production rate of $Ni_{0.04}Cu$ was measured to be 878.4 μmol $g_{catalyst}^{-1}$ min^{-1}, which is nearly 3.3 times over the reaction rate under dark condition. After the reaction temperature increased to 210 °C with visible light irradiation, the reaction rate of $Ni_{0.04}Cu$ increased to 2140.7 μmol $g_{catalyst}^{-1}$ min^{-1}, which is higher than pure Cu (1073 μmol $g_{catalyst}^{-1}$ min^{-1}) at the same reaction condition. These results indicated that the visible light energy could facilitate the ethanol dehydrogenation activity. Steady-state reaction hydrogen production rate at a temperature of 200 °C (Figure 3b) showed that the H_2 production rate increased by ~2 times after the photon energy was introduced, while decreased back to 900 μmol $g_{catalyst}^{-1}$ min^{-1} after the illuminate was removed, suggesting that the dehydrogenation of ethanol reaction over $Ni_{0.04}Cu$ was light-sensitive. The photo-enhancement in activity showed superiority at low temperature, since the enhancement for H_2 production rate of $Ni_{0.04}Cu$ (calculated by the rate with light irradiation divided by the rate in dark condition) declined from 3.3 to 1.7 times with the temperature increasing from 170 to 210 °C (Figure S10). The rate difference of $Ni_{0.04}Cu$ was also calculated by the reaction rate with light irradiated minus the reaction rate in dark conditions. Figure S11 showed that the rate difference of $Ni_{0.04}Cu$ increased with the increasing reaction temperature before 200 °C, and then decreased. Moreover, as shown from Figure S12, the $Ni_{0.04}Cu$ catalysts displayed good stability under dark and light conditions in 5-hour reaction. Compared with $Ni_{0.04}Cu$, pure Ni demonstrated lower activity and severe deactivation (Figure S13).

The visible light intensity dependent H_2 production rate was carried out to identify the mechanism for enhanced photocatalytic activity of $Ni_{0.04}Cu$, and the result showed

that the reaction rate presented a linear dependence on the light intensity, indicating that the hot carriers induced by visible light played a critical role in the photo-enhanced ethanol dehydrogenation reaction over $Ni_{0.04}Cu$ catalysts (Figure 3c) [24, 25]. To verify the enhanced activity was attributed to the LSPR effect of Cu, the impact of different irradiation wavelengths on the reaction rate of $Ni_{0.04}Cu$ catalysts were measured. The monochromatic light filter (MIF-W type 470, 520, 570, 620 nm) coupled with HA30 and L42 filters were utilized in reaction to obtain the desired wavelength range. By the irradiation of light, $Ni_{0.04}Cu$ showed a broad absorption peak of around 580 nm, which could be attributed to the LSPR peak of Cu. The tendency of apparent quantum efficiency (AQE) of $Ni_{0.04}Cu$ catalysts were consistent with its optical absorption spectrum, indicating that the enhancement of photocatalytic activity was attributed to the excitation of hot carriers. The hot electrons induced by a wavelength of 620 nm might be not energetic enough for realizing ethanol dehydrogenation reaction (Figure 3d).

The reaction kinetics of the ethanol dehydrogenation reaction under dark and with light irradiation at a reaction temperature from 170-210 °C were investigated to understand the underlying reaction mechanism. The apparent activation energy was calculated by fitting the reaction rates by using the Arrhenius equation ($\ln r = -E_a/RT + \ln A$), as shown in Figure 3e. The apparent activation energy of pure Cu in the dark condition was 92.4 kJ mol^{-1}, and it decreased to 61.2 kJ mol^{-1} under the visible light irradiation, indicating that the visible light could provide additional energy for the surface reaction to reduce the apparent activation energy. The apparent activation energy was further reduced when a little amount of Ni was deposited on the surface of Cu. As shown in Figure 3e, $Ni_{0.04}Cu$ exhibited an activation energy of 67.4 kJ mol^{-1} even without light irradiation. Under the visible light irradiation, the apparent activation energy of $Ni_{0.04}Cu$ remarkably decreased to 41.5 kJ mol^{-1}, demonstrating that photo-induced hot carriers greatly assisted the dehydrogenation process of ethanol.

In situ DRIFT spectra were employed to further investigate the effect of hot carriers on ethanol dehydrogenation reaction. Figure 3f showed the infrared (IR) absorption

spectra of $Ni_{0.04}Cu$ with ethanol at 200 °C under dark and light conditions. Based on the literature results, the sharp bands at 3744 cm^{-1} could be attributed to the isolated silanol groups [46], whereas the features centered at 3670 cm^{-1} and 1250 cm^{-1} were assigned to O-H stretching and bending frequencies [47]. Two dominant peaks at 2985 cm^{-1} and 2905 cm^{-1} could be attributed to CH_3 and CH_2 asymmetric stretching [34]. The peak centered at 1050 cm^{-1} was characteristic of C-O stretching [47]. Comparatively, upon light irradiation, the intensity of each peak was substantially attenuated, indicating that a more facile activation of the adsorbed intermediates could be achieved with the aid of photo-induced hot carriers. Since the most peaks of ethoxy species (CH_3CH_2O*) and molecularly adsorbed ethanol (CH_3CH_2OH*) overlapped, it was difficult to distinguish from IR spectra. However, the presence of OH peak (1250 and 3670 cm^{-1}) indicated that the adsorbed ethanol was a stable and dominant intermediate. Upon the light irradiation, the intensity of O-H stretching and bending frequencies (1250 and 3670 cm^{-1}) decreased obviously, indicating the formation of more ethoxy intermediates (CH_3CH_2O*). The adsorbed ethoxy species could lose one hydrogen atom to form acetaldehyde or it could gradually lose more hydrogen atoms by sequential C-H bond scission. Meanwhile, two peaks at 1723 and 1756 cm^{-1}, associated with C=O stretching vibration of acetaldehyde, were observed after introducing light [47]. In addition, the broad peak at 2728 cm^{-1} also indicated the generation of acetaldehyde upon light irradiation [47].

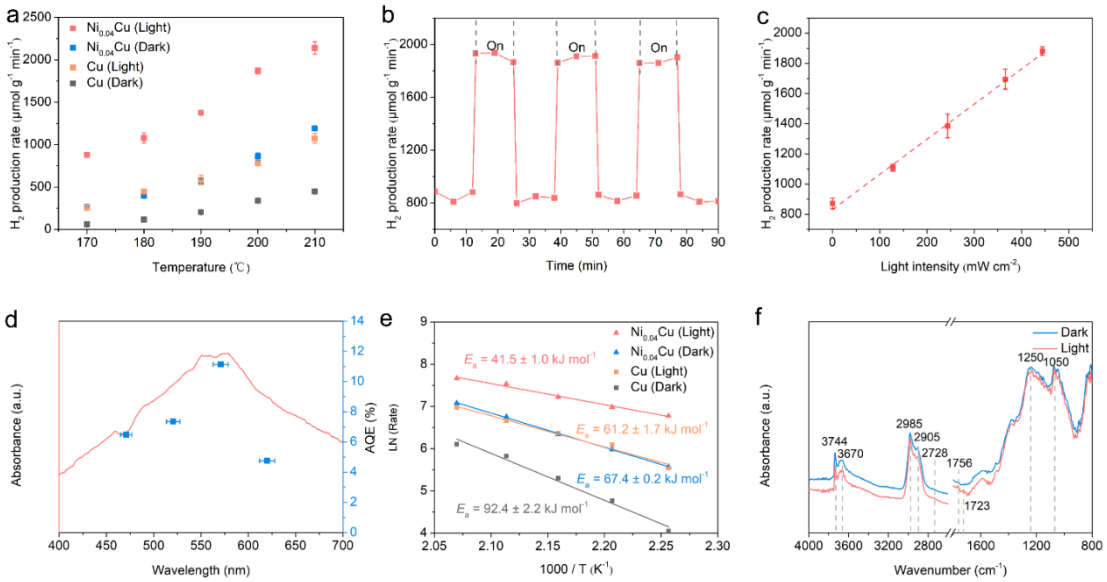

Figure 3. Mechanistic investigation for hot carriers assisted ethanol dehydrogenation reaction. (a) Reaction rate of H_2 production on the Cu and Ni-Cu bimetallic catalysts as a function of temperature under the purely thermal condition (dark) and under photo-assisted thermal condition (light), (b) H_2 production rate on $Ni_{0.04}Cu$ catalyst with and without visible light irradiation at 200 °C, (c) Dependence of H_2 production rate of $Ni_{0.04}Cu$ at 200 °C on light intensity, (d) Light absorption and AQE values of $Ni_{0.04}Cu$ at 200 °C with light irradiation in different wavelength ranges, (e) Arrhenius plots for H_2 production rate under dark and light conditions over pure Cu and $Ni_{0.04}Cu$ catalysts, error bars represent the standard deviation of three measurements with the same catalysts, (f) *In-situ* DRIFT spectra of $Ni_{0.04}Cu$ catalysts under dark and light conditions.

3.4 First-principles molecular dynamics simulation

In the limited duration time of simulation (i.e. less than a few picoseconds) at around 200 °C, no stable adsorption of ethanol molecule on the Ni-doped Cu metallic slab surface was observed, although ethanol molecules often collided with the surface. It was implied that the system was thermally mild for reactant molecules. To save a computational cost although much longer-term simulation might bring us spontaneous molecular dissociation, one of the ethanol molecules was manually decomposed into

CH_3CHO and 2 H atoms near the metallic slab surface. Then, the molecular dynamics of the system were observed for a picosecond. It was found that the CH_3CHO molecule moved away from the near-surface to the free space, but the H atoms were strongly adsorbed to surficial metallic atoms.

Figure 4 showed (a) the snapshot of the thermal equilibrium structure of the system, (b) the local structure of proton-metal adsorbate (-M-H), and (c) - (m) the electronic properties of the Cu slab doped with Ni on which -H are adsorbed in presence of one acetaldehyde and three ethanol molecules when one of ethanol molecule collides with the surface. Each detailed weight profile (c) - (m) of atomic orbital wavefunction components was obtained by projecting the eigen-wave-function onto the corresponding atomic orbital(s). The atomic distances of Cu-H and Ni-H fluctuated in the range roughly 1.7~2.0 Å and 1.6~1.8 Å and those at the moment of the snapshot in the Figure 4 (b) were 1.78 Å, 1.81 Å, and 1.65 Å, respectively. In the electronic properties [48, 49], only significant components were presented. The electrons in the system occupied up to -4.25 eV as indicated by the black solid line in (c ~ m). The occupied states were spanned mostly by Cu 3d ((c) for all 184 Cu atoms) and 4s ((d) for all 184 Cu atoms) orbitals components and the unoccupied states in the energy range from -4.25 to -2 eV were also composed dominantly of the Cu 3d and 4s orbitals. Investigating the components of the unoccupied Ni 3d ((e) for all 8 Ni atoms) states and the unoccupied H 1s states in the metallic atom - proton adsorbates (-M-H), some interesting electronic properties were found. Unoccupied Ni 3d band was situated in the energy range from -4.25 roughly to -2 eV (dominantly from -4.25 to -3 eV) and, at the same time, the unoccupied H 1s component ((f) for just one H atom (Figure 4 (b)) of the dissociated two H atoms (a)) originating from the absorbed -H on the Cu-based metallic slab were also located mainly in the range from -3.7 to -2.9 eV as underlined in pale orange, which was just around the Ni 3d band. Based on the electronic properties, it could be elucidated that the electrons in 3d and 4s orbitals of Cu were excited to the unoccupied 3d and 4s orbitals of Cu under visible light irradiation and simultaneously the energetic electrons could be distributed to the unoccupied 3d band of Ni, and further

transferred into the unoccupied H 1s orbitals of the -Cu-H-Ni- adsorbates. Further detailed electronic properties on the local area of the -Cu-H-Ni- adsorbate (Figure 4b) were presented in Figure 4 (j) - (m) using the same transverse range for easy direct comparison. It indicated that the unoccupied H1s band was hybridized with the unoccupied Ni 3d band much better than with the unoccupied Cu 3d band or Cu 4s band. Therefore, the photo-excited hot electrons were easily transferred to the proton adsorbed at the surface with suppressing the non-effective carrier recombination, leading to the promotion of H_2 production.

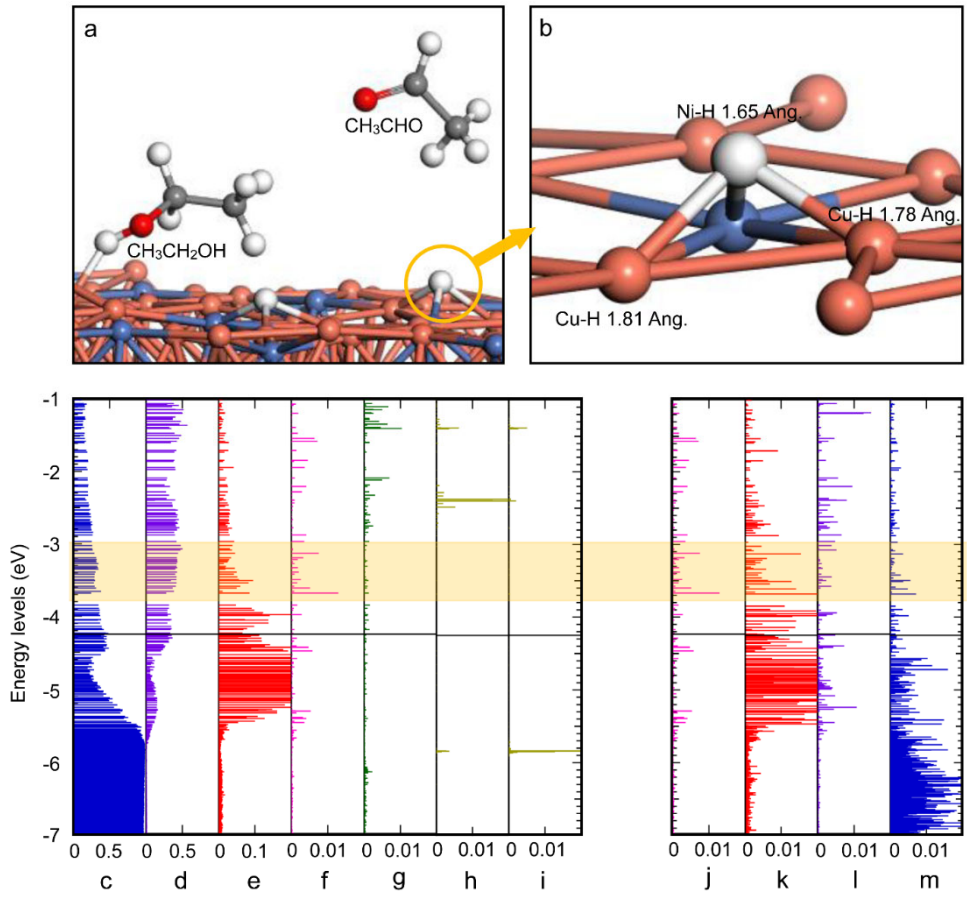

Figure 4. First-principles molecular dynamics simulation of $Ni_{0.04}Cu$ in the reaction molecular of CH_3CH_2OH and CH_3CHO. (a) Snapshot of the equilibrium structure at 200 °C of the Cu metal doped with Ni atoms, which is intended to mimic $Cu_{1-\delta}Ni_{\delta}/SiO_2$ systems, in the presence of ethanol and acetaldehyde molecules. The color code is white for H, red for O, gray for C, brown for Cu, and cyan for Ni, (b) Local adsorbate structure

of -Ni-H-Cu- at the slab surface, (c-m) Corresponding electronic structures of the system, (c) Cu 3d, (d) Cu 4s, (e) Ni 3d, (f) H 1s at the surface, (g) H 1s of all H in CH_3CH_2OH colliding with the surface, (h) H 1s of all H of -CH_3 in CH_3CHO, (i) H 1s of -CHO in CH_3CHO, (j) H 1s at the surface, (k) Ni 3d of -Ni-H 1.65 Ang. at the surface, (l) Cu 4s of -Cu-H 1.78 Ang. at the surface, (m) Cu 3d of -Cu-H 1.78 Ang. at the surface; Black solid line indicates the Fermi level.

Conclusion

In summary, our study demonstrated that ethanol dehydrogenation for the production of H_2 and acetaldehyde could be efficiently driven by focused solar light over Ni-Cu bimetallic catalysts. High solar-to-fuel conversion efficiency of 3.81% and hydrogen production rate (2943 μmol $g_{catalyst}^{-1}$ min^{-1}) could be achieved under simulated 5.7 Suns irradiation without any additional thermal energy input. Mechanistic investigations revealed that the synergistic effects of photothermal heating and hot carrier generation through the excitation of surface plasmon resonance over Ni-Cu bimetallic catalysts played critical roles for the observed high activity and decreased activation energy. First-principles molecular dynamics simulation revealed that the hot electrons were generated from Cu and migrated to Ni atom, facilitating the formation of hydrogen and suppressing the non-effective carrier recombination. This study provides a new promising strategy to activate industrial useful and tough reactions by using renewable solar energy and the construction of efficient plasmonic photocatalysts.

Acknowledgement

This work was financially supported by JSPS KAKENHI (No. JP18H02065), the Photo-excitonix Project at Hokkaido University, the World Premier International Research Center Initiative (WPI Initiative) on Materials Nanoarchitectonics (MANA), MEXT (Japan), National Natural Science Foundation of China (No. 21633004), State Scholarship Fund by China Scholarship Council (CSC) (No. 201806400044 and No. 201606320239).

Reference

[1] M.Z. Jacobson, W.G. Colella, D.M. Golden, Cleaning the Air and Improving Health with Hydrogen Fuel-Cell Vehicles, Science. 308 (2005) 1901-1905.

[2] I. Staffell, D. Scamman, A. Velazquez Abad, P. Balcombe, P.E. Dodds, P. Ekins, N. Shah, K.R. Ward, The role of hydrogen and fuel cells in the global energy system, Energ. Environ. Sci. 12 (2019) 463-491.

[3] L. Zhao, Y. Qi, L. Song, S. Ning, S. Ouyang, H. Xu, J. Ye, Solar-Driven Water-Gas Shift Reaction over CuOx /Al_2O_3 with 1.1% of Light-to-Energy Storage, Angew. Chem. Int. Ed. 58 (2019) 7708-7712.

[4] S.T. Wismann, J.S. Engbæk, S.B. Vendelbo, F.B. Bendixen, W.L. Eriksen, K. Aasberg-Petersen, C. Frandsen, I. Chorkendorff, P.M. Mortensen, Electrified methane reforming: A compact approach to greener industrial hydrogen production, Science. 364 (2019) 756-759.

[5] B. Wang, S. He, L. Zhang, X. Huang, F. Gao, W. Feng, P. Liu, CdS nanorods decorated with inexpensive NiCd bimetallic nanoparticles as efficient photocatalysts for visible-light-driven photocatalytic hydrogen evolution, Appl. Catal. B-Environ. 243 (2019) 229-235.

[6] U. Caudillo-Flores, M.J. Muñoz-Batista, M. Fernández-García, A. Kubacka, Bimetallic Pt-Pd co-catalyst Nb-doped TiO_2 materials for H_2 photo-production under UV and Visible light illumination, Appl. Catal. B-Environ. 238 (2018) 533-545.

[7] A.V. Puga, A. Forneli, H. García, A. Corma, Production of H_2 by Ethanol Photoreforming on Au/TiO_2, Adv. Funct. Mater. 24 (2014) 241-248.

[8] A. Segawa, A. Nakashima, R. Nojima, N. Yoshida, M. Okamoto, Acetaldehyde Production from Ethanol by Eco-Friendly Non-Chromium Catalysts Consisting of Copper and Calcium Silicate, Ind. Eng. Chem. Res. 57 (2018) 11852-11857.

[9] P. Liu, E.J. Hensen, Highly efficient and robust Au/$MgCuCr_2O_4$ catalyst for gas-phase oxidation of ethanol to acetaldehyde, J. Am. Chem. Soc. 135 (2013) 14032-14035.

[10] E. Taboada, I. Angurell, J. Llorca, Dynamic photocatalytic hydrogen production from ethanol–water mixtures in an optical fiber honeycomb reactor loaded with Au/TiO_2, J. Catal. 309 (2014) 460-467.

[11] M.J. Sampaio, J.W.L. Oliveira, C.I.L. Sombrio, D.L. Baptista, S.R. Teixeira, S.A.C. Carabineiro, C.G. Silva, J.L. Faria, Photocatalytic performance of Au/ZnO nanocatalysts for hydrogen production from ethanol, Appl. Catal. A-Gen. 518 (2016) 198-205.

[12] X. Zhang, L. Luo, R. Yun, M. Pu, B. Zhang, X. Xiang, Increasing the Activity and Selectivity of TiO_2-Supported Au Catalysts for Renewable Hydrogen Generation from Ethanol Photoreforming by Engineering Ti^{3+} Defects, ACS Sustain. Chem. Eng. 7 (2019) 13856-13864.

[13] C. Lu, J. Li, G. Chen, B. Li, Z. Lou, Self-Z-scheme plasmonic tungsten oxide nanowires for boosting ethanol dehydrogenation under UV-visible light irradiation, Nanoscale. 11 (2019) 12774-12780.

[14] M. Murdoch, G. I. Waterhouse, M. A. Nadeem, J. B. Metson, M. A. Keane, R. F. Howe, J. Llorca, H. Idriss, The effect of gold loading and particle size on photocatalytic hydrogen production from ethanol over Au/TiO_2 nanoparticles, Nat. Chem. 3 (2011) 489-492.

[15] C. Kim, B.L. Suh, H. Yun, J. Kim, H. Lee, Surface Plasmon Aided Ethanol Dehydrogenation Using Ag–Ni Binary Nanoparticles, ACS Catal. 7 (2017) 2294-2302.

[16] L. Zhou, D.F. Swearer, C. Zhang, H. Robatjazi, H. Zhao, L. Henderson, L. Dong, P. Christopher, E.A. Carter, P. Nordlander, N.J. Halas, Quantifying hot carrier and thermal contributions in plasmonic photocatalysis, Science. 362 (2018) 69-72.
[17] H. Robatjazi, H. Zhao, D.F. Swearer, N.J. Hogan, L. Zhou, A. Alabastri, M.J. McClain, P. Nordlander, N.J. Halas, Plasmon-induced selective carbon dioxide conversion on earth-abundant aluminum-cuprous oxide antenna-reactor nanoparticles, Nat. Commun. 8 (2017) 27.
[18] D. Gao, W. Liu, Y. Xu, P. Wang, J. Fan, H. Yu, Core-shell Ag@Ni cocatalyst on the TiO_2 photocatalyst: One-step photoinduced deposition and its improved H_2-evolution activity, Appl. Catal. B-Environ. 260 (2020) 118190.
[19] X. Meng, L. Liu, S. Ouyang, H. Xu, D. Wang, N. Zhao, J. Ye, Nanometals for Solar-to-Chemical Energy Conversion: From Semiconductor-Based Photocatalysis to Plasmon-Mediated Photocatalysis and Photo-Thermocatalysis, Adv. Mater. 28 (2016) 6781-6803.
[20] Z.J. Wang, H. Song, H. Liu, J. Ye, Coupling of Solar Energy and Thermal Energy for Carbon Dioxide Reduction: Status and Prospects, Angew. Chem. Int. Ed. 59 (2020), 2-22.
[21] M. Ghoussoub, M. Xia, P.N. Duchesne, D. Segal, G. Ozin, Principles of photothermal gas-phase heterogeneous CO_2 catalysis, Energ. Environ. Sci. 12 (2019) 1122-1142.
[22] M.Q. Yang, L. Shen, Y. Lu, S.W. Chee, X. Lu, X. Chi, Z. Chen, Qi.H. Xu, U. Mirsaidov, G.W. Ho, Disorder Engineering in Monolayer Nanosheets Enabling Photothermic Catalysis for Full Solar Spectrum (250-2500 nm) Harvesting, Angew. Chem. Int. Ed. 58 (2018) 3077-3081.
[23] S. Kim, J.M. Kim, J.E. Park, J.M. Nam, Nonnoble-Metal-Based Plasmonic Nanomaterials: Recent Advances and Future Perspectives, Adv. Mater. 30 (2018) 1704528.
[24] H. Song, X. Meng, Z.J. Wang, Z. Wang, H. Chen, Y. Weng, F. Ichihara, M. Oshikiri, T. Kako, J. Ye, Visible-Light-Mediated Methane Activation for Steam Methane Reforming under Mild Conditions: A Case Study of Rh/TiO_2 Catalysts, ACS Catal. 8 (2018) 7556-7565.
[25] H. Song, X. Meng, T.D. Dao, W. Zhou, H. Liu, L. Shi, H. Zhang, T. Nagao, T. Kako, J. Ye, Light-Enhanced Carbon Dioxide Activation and Conversion by Effective Plasmonic Coupling Effect of Pt and Au Nanoparticles, ACS Appl. Mater. Inter. 10 (2018) 408-416.
[26] H. Song, X. Meng, Z.-j. Wang, H. Liu, J. Ye, Solar-Energy-Mediated Methane Conversion, Joule, 3 (2019) 1606-1636.
[27] U. Aslam, V.G. Rao, S. Chavez, S. Linic, Catalytic conversion of solar to chemical energy on plasmonic metal nanostructures, Nat. Catal. 1 (2018) 656-665.
[28] X.Y. Gan, E.L. Keller, C.L. Warkentin, S.E. Crawford, R.R. Frontiera, J.E. Millstone, Plasmon-Enhanced Chemical Conversion Using Copper Selenide Nanoparticles, Nano Lett. 19 (2019) 2384-2388.
[29] J. Chen, J. Feng, F. Yang, R. Aleisa, Q. Zhang, Y. Yin, Space-Confined Seeded Growth of Cu Nanorods with Strong Surface Plasmon Resonance for Photothermal Actuation, Angew. Chem. Int. Ed. 58 (2019) 9275-9281.
[30] J. Jiao, R. Lin, S. Liu, W.C. Cheong, C. Zhang, Z. Chen, Y. Pan, J. Tang, K. Wu, S.F. Hung, H.M. Chen, L. Zheng, Q. Lu, X. Yang, B. Xu, H. Xiao, J. Li, D. Wang, Q. Peng, C. Chen, Y. Li, Copper atom-pair catalyst anchored on alloy nanowires for selective and efficient electrochemical reduction of CO_2, Nat Chem. 11 (2019) 222-228.
[31] A. Carrero, J.A. Calles, A.J. Vizcaíno, Hydrogen production by ethanol steam reforming over Cu-Ni/SBA-15 supported catalysts prepared by direct synthesis and impregnation, Appl. Catal. A-Gen. 327 (2007) 82-94.

[32] J. Shan, N. Janvelyan, H. Li, J. Liu, T.M. Egle, J. Ye, M.M. Biener, J. Biener, C.M. Friend, M. Flytzani-Stephanopoulos, Selective non-oxidative dehydrogenation of ethanol to acetaldehyde and hydrogen on highly dilute NiCu alloys, Appl. Catal. B-Environ. 205 (2017) 541-550.
[33] M.D. Marcinkowski, M.T. Darby, J. Liu, J.M. Wimble, F.R. Lucci, S. Lee, A. Michaelides, M. Flytzani-Stephanopoulos, M. Stamatakis, E.C.H. Sykes, Pt/Cu single-atom alloys as coke-resistant catalysts for efficient C-H activation, Nat Chem. 10 (2018) 325-332.
[34] J. Shan, J. Liu, M. Li, S. Lustig, S. Lee, M. Flytzani-Stephanopoulos, NiCu single atom alloys catalyze the C-H bond activation in the selective non-oxidative ethanol dehydrogenation reaction, Appl. Catal. B-Environ. 226 (2018) 534-543.
[35] H. Huang, M. Mao, Q. Zhang, Y. Li, J. Bai, Y. Yang, M. Zeng, X. Zhao, Solar-Light-Driven CO_2 Reduction by CH_4 on Silica-Cluster-Modified Ni Nanocrystals with a High Solar-to-Fuel Efficiency and Excellent Durability, Adv. Energy Mater. 8 (2018) 1702472-1702482.

[36] D.R. Lide, CRC Handbook of Chemistry and Physics, 84th Edition, CRC Handbook of Chemistry and Physics, 84th Edition, (2003).
[37] R. Car, M. Parrinello, Unified approach for molecular dynamics and density-functional theory, Phys. Rev. Lett. 55 (1985) 2471-2474.
[38] A. Marimuthu, J. Zhang, S. Linic, Tuning selectivity in propylene epoxidation by plasmon mediated photo-switching of Cu oxidation state, Science. 339 (2013) 1590-1593.
[39] B. Qiao, A. Wang, X. Yang, L.F. Allard, Z. Jiang, Y. Cui, J. Liu, J. Li, T. Zhang, Single-atom catalysis of CO oxidation using Pt_1/FeOx, Nat. Chem. 3 (2011) 634-641.
[40] Z. Zhang, Y. Zhu, H. Asakura, B. Zhang, J. Zhang, M. Zhou, Y. Han, T. Tanaka, A. Wang, T. Zhang, N. Yan, Thermally stable single atom Pt/m-Al_2O_3 for selective hydrogenation and CO oxidation, Nat. Commun. 8 (2017) 16100.
[41] L. Wang, W. Zhang, S. Wang, Z. Gao, Z. Luo, X. Wang, R. Zeng, A. Li, H. Li, M. Wang, X. Zheng, J. Zhu, W. Zhang, C. Ma, R. Si, J. Zeng, Atomic-level insights in optimizing reaction paths for hydroformylation reaction over Rh/CoO single-atom catalyst, Nat. Commun. 7 (2016) 14036.
[42] H. Li, L. Wang, Y. Dai, Z. Pu, Z. Lao, Y. Chen, M. Wang, X. Zheng, J. Zhu, W. Zhang, R. Si, C. Ma, J. Zeng, Synergetic interaction between neighbouring platinum monomers in CO_2 hydrogenation, Nat. Nanotechnol. 13 (2018) 411-417.
[43] X. Fang, Q. Shang, Y. Wang, L. Jiao, T. Yao, Y. Li, Q. Zhang, Y. Luo, H.L. Jiang, Single Pt Atoms Confined into a Metal-Organic Framework for Efficient Photocatalysis, Adv. Mater. 30 (2018) 1705112-1705118.
[44] N.D. Subramanian, C.S.S.R. Kumar, K. Watanabe, P. Fischer, R. Tanaka, J.J. Spivey, A DRIFTS study of CO adsorption and hydrogenation on Cu-based core-shell nanoparticles, Catal. Sci. Technol. 2 (2012) 621–631.
[45] S.F. Moya, R.L. Martins, M. Schmal, Monodispersed and nanostructrured Ni/SiO_2 catalyst and its activity for non oxidative methane activation, Appl. Catal.A-Gen. 396 (2011) 159-169.
[46] V.L. Sushkevich, I.I. Ivanova, E. Taarning, Mechanistic Study of Ethanol Dehydrogenation over Silica-Supported Silver, ChemCatChem. 5 (2013) 2367-2373.
[47] A. Kumar, A. Ashok, R.R. Bhosale, M.A.H. Saleh, F.A. Almomani, M. Al-Marri, M.M. Khader, F. Tarlochan, In situ DRIFTS Studies on Cu, Ni and CuNi catalysts for Ethanol Decomposition Reaction, Catal. Lett., 146 (2016) 778-787.

[48] B.G. Johnson, P.M.W. Gill, J.A. Pople, The performance of a family of density functional methods, J. Chem. Phys. 98 (1993) 5612-5626.
[49] M. Oshikiri, J. Ye, M. Boero, Inhomogeneous RVO4 Photocatalyst Systems (R = Y, Ce, Pr, Nd, Sm, Eu, Gd, Tb, Dy, Ho, Er, Tm, Yb, Lu), J. Phys. Chem. C. 118 (2014) 8331-8341.